

## Formation of copper nanoparticles in mordenites with variable $\text{SiO}_2/\text{Al}_2\text{O}_3$ molar ratios under redox treatments

V. Petranovskii<sup>a,\*</sup>, E. Stoyanov<sup>b</sup>, V. Gurin<sup>c</sup>, N. Katada<sup>d</sup>, M.-A. Hernandez<sup>e</sup>, M. Avalos<sup>a</sup>, A. Pestryakov<sup>f</sup>,  
F. Chávez Rivas<sup>g</sup>, R. Zamorano Ulloa<sup>g</sup>, and R. Portillo<sup>h</sup>

<sup>a</sup> Centro de Nanociencias y Nanotecnología, Universidad Nacional Autónoma de México,  
km 107 carretera Tijuana-Ensenada, Ensenada 22800, B.C., México.

\*Postal address: CNYN-UNAM, P.O. Box 439036, San Ysidro, CA 92143, USA

Tel.: +52(646)-174-4602; fax: +52(646)-174-4603.

e-mail address: vitalii@cnyun.unam.mx

<sup>b</sup>Department of Chemistry, University of California, Riverside, California 92521.

<sup>c</sup>Research Institute for Physical Chemical Problems, Belarusian State University, Minsk 220080, Belarus.

<sup>d</sup>Department of Chemistry and Biotechnology, Tottori University, Tottori 680-8552, Japan.

<sup>e</sup>Departamento de Investigación en Zeolitas, Universidad Autónoma de Puebla, Puebla, México.

<sup>f</sup> Tomsk Polytechnic University, Tomsk 634050, Russia

<sup>g</sup> Departamento de Física ESFM-IPN,

Zacatenco, 07738. México, D.F.

<sup>h</sup> Facultad de Ciencias Químicas, Universidad Autónoma de Puebla, Puebla, México.

Received 14 August 2012; accepted 13 December 2012

A series of protonated copper-containing mordenites with different  $\text{SiO}_2/\text{Al}_2\text{O}_3$  molar ratios (MR) in the range of  $10 \leq \text{MR} \leq 206$  was prepared by ion exchange in copper nitrate aqueous solution. The electron paramagnetic resonance of hydrated copper Mordenites series testifies of several  $\text{Cu}^{2+}$  ions sites. Hydrogen reduction of copper ions incorporated into the mordenites was shown to lead to different reduced copper species including small metallic particles *inter alia*. The structural properties and acidity of mordenites were characterized. The optical appearance of the copper particles showed strong but nonmonotonic dependence on the MR value, in line with the variation in acidity of this series of mordenites. Correlations between mordenite properties and the formation of different reduced copper species are discussed.

**Keywords:** Mordenite;  $\text{SiO}_2/\text{Al}_2\text{O}_3$  molar ratio; Copper; Nanoparticles; Plasmon resonance

Un conjunto de zeolitas mordenitas protonadas e intercambiadas con cobre y con diferentes relaciones molares (RM) de  $\text{SiO}_2/\text{Al}_2\text{O}_3$  en el intervalo  $10 \leq \text{MR} \leq 206$  ha sido preparado por intercambio iónico en solución acuosa de nitrato de cobre. La resonancia paramagnética electrónica del conjunto de mordenitas con cobre en su estado hidratado muestra varios sitios de iones  $\text{Cu}^{2+}$ . La reducción por hidrógeno de los iones de cobre incorporados en las mordenitas ha demostrado que la reducción produce diferentes especies de cobre, incluyendo la reducción de pequeñas partículas metálicas *inter alia*. Se han caracterizado las propiedades estructurales y la acidez del conjunto de mordenitas intercambiadas. La señal óptica de nanopartículas de cobre mostró fuerte dependencia monotónica, pero no con el valor RM, en línea con la variación de la acidez de este conjunto de mordenitas. Las correlaciones entre las propiedades de las mordenitas y la formación de diferentes especies reducidas de cobre son discutidas.

**Descriptores:** Mordenita; relación molar  $\text{SiO}_2/\text{Al}_2\text{O}_3$ ; Cobre; EPR; Nanopartículas; Resonancia Plasmónica.

PACS: 78.67.Sc; 76.30.-v; 78.40.-q

### 1. Introduction

Transition metals incorporated into solid matrices are widely used in the preparation of catalysts and nanocomposites with unusual optical, electrical and magnetic properties. Such materials have been extensively studied during recent years. The presence of metal in ionic form or as small clusters and nanoparticles in the host matrices drastically changes the properties of these composite materials even if the dopants are present at low concentrations. As regards zeolites, their ion exchange properties permit introduction of metal into zeolite voids, while subsequent reduction leads to different reduced metal species [1-3]. The multicomponent metal-dielectric systems produced by incorporation of metal into zeolites are of special interest concerning the metal-support

interaction, and to understand the mutual contribution of different components to the properties of the whole system. Zeolites possess molecular sieving properties due to the well-defined size of their pore openings. This feature can lead to additional stabilization of small clusters whose size matches the inner space of zeolite channels [4-9]. A great variety of natural and synthetic zeolites with controllable properties and different crystal structures are known [10,11]. Unlike some matrices used for incorporation of metals, zeolites not only provide mechanical support for topological reasons, but are also an active ionic medium which promotes a rich chemistry of metal ions. These are incorporated at specific sites in zeolite crystals, together with other accompanying reagents, like water for example, and interact with other exchangeable ions and/or with the different Brønsted and Lewis acid sites [10].

Further chemical transformations with metal-zeolite systems (redox processes, dehydration, metal particle aggregation, etc.) generate new nanocomposites with complicated structures in which the properties of matrix, incorporated metal and metal-matrix interactions all play a role.

Copper-containing zeolites are of particular interest due to their catalytic activity in *de*NO<sub>x</sub> reactions [12-14]. Although these compounds received considerable attention during the last decade, there is still ambiguity about the interpretation of certain copper species in different zeolites. Metal ion distribution within these matrices strongly depends on the different conditions of metal incorporation, and the effect of subsequent processes such as heat treatment of Cu-zeolites in different atmospheres adds to the complex final structure of these composites.

It has been stated that the SiO<sub>2</sub>/Al<sub>2</sub>O<sub>3</sub> molar ratio (MR) is the key-factor governing formation and relative stability of silver clusters in mordenites. Changing the chemical composition of the mordenite framework (*i.e.*, changing the MR, and, consequently, the acidity that depends on the MR) leads to non-monotonic dependence of cluster stabilization on MR [15,16]. The MR value of Cu-mordenite is one of the crucial characteristics enhancing the hydrothermal stability of NO reduction catalysts under lean NO<sub>x</sub> wet conditions [17]. Analysis by the Monte Carlo procedure shows that the distinct distribution of Al atom pairs in -O-Al-O-(Si-O)<sub>n</sub>-Al-O- fragments in mordenite creates sites that provide favorable binding environments for extra-framework Cu<sup>2+</sup> cations; this distribution of Al atoms is determined by the SiO<sub>2</sub>/Al<sub>2</sub>O<sub>3</sub> ratio [18]. Thus, the coordination, localization and stabilization of copper ions in zeolitic materials strongly depend on the structure and composition of the zeolite matrix. The mordenite framework possesses several positions for the localization of cations in general, as well as for copper ions [10,19,20]. In this way, the solid zeolite matrix plays the role of a substrate with a range of polydentate ligands for Cu<sup>2+</sup>. Since the *redox* behavior of the Cu<sup>2+</sup>/Cu<sup>+</sup>/Cu<sup>0</sup> system is very sensitive not only to the medium but also to the complexation of copper by different ligands, this should lead to the appearance of different copper states in zeolites.

The aim of the present work was to investigate how acidity, secondary porosity and local structure features of mordenites depend on the MR, and how reduction temperature during treatment in hydrogen influences the optical appearance of reduced copper species in these matrices.

The copper state in mordenite samples was detected by means of electron paramagnetic resonance (EPR) absorption and UV/Vis absorption using diffuse reflectance spectroscopy (DRS), the EPR technique gives information mainly of spin transitions of Cu<sup>2+</sup> ions and the UV/Vis-DRS technique is a convenient method to obtain optical information on opaque (powder-like) materials. The contribution of different copper states is known to be rather pronounced in the UV/Vis-DRS spectra, which allowed us to identify their appearance in the series of copper ionexchanged and reduced mordenites.

The plan of this work is as follows. Section 2 shortly describes the experimental procedures and devices. Section 3.1 provides a structural characterization of the used set of mordenites, and explains the method to determine their acid properties. ESR spectra of hydrated samples are discussed in the Secs. 3.2. From this EPR study we have found different Cu<sup>2+</sup> ions sites in the set of the unreduced samples with a relative estimation of the amount of Cu<sup>2+</sup> ions in each sample. Sections 3.3 and 3.4 offer a detailed analysis of the experimental data obtained by DRS of the series of samples under study. We show the original mordenites, the copper-ion-exchanged composites and the reduced mordenites with copper. The behavior of mordenites with different MR appears to be markedly different, and we therefore consider them separately, summarizing obtained data in Sec. 3.5 and incorporating into the discussion our data on theoretical estimation of the spectral appearance of reduced copper [21,22]. Section 4 concludes the Discussion and sums up the main results.

## 2. Experimental

Protonated forms of mordenites with MR varying from 10 to 206 were supplied by TOSOH Corporation, Japan. Copper ion exchange was carried out at ambient temperature from 0.1 N Cu(NO<sub>3</sub>)<sub>2</sub> aqueous solution for 24 h under constant stirring in excess of Cu<sup>2+</sup>. The samples were filtered, washed and dried under ambient conditions followed by heating in a dry H<sub>2</sub> flow at temperatures from 150 to 450°C for 4 h. The copper content in the prepared samples was determined by atomic absorption spectrometry using Varian model 1475 equipment.

Surface area  $S_{BET}$  and pore volume  $V_{\Sigma}$  were determined by high-resolution nitrogen adsorption measurements on an Autosorb-1 Quantachrome equipment in the range of  $10^{-6} < p/p_0 < 1$ . The crystallinity and the cell constants were monitored by X-ray diffraction (XRD) measurements on a Philips diffractometer, model X'Pert, equipped with a curved graphite monochromator, using Cu K<sub>α</sub> radiation. Diffuse reflectance spectra (DRS) were collected on a Varian Cary 300 equipped with a standard diffuse reflectance unit using a barium sulfate reference in the wavelength range 190-850 nm. The spectra were obtained in air just after cooling the hydrogen-treated samples.

The Brønsted acidity of the mordenite surface was studied using the method of non-aqueous potentiometric titration of the suspension of desiccated mordenites in anhydrous dimethylformamide medium by ethyl alcohol solution of C<sub>2</sub>H<sub>5</sub>OK, using a pH673M potentiometer with platinum and glass electrodes.

Temperature Programmed Desorption (TPD) measurements with ammonia were performed using a TPD-1-AT Bell Japan Inc. equipment and analyzed according to [23]. The zeolite sample (0.1 g) was packed into a quartz cell. It was evacuated at 773 K for 1 h, followed by ammonia adsorption (13.3 kPa) at 373 K. Weakly held ammonia was removed by water vapor treatment [24]. Finally, the zeolite bed was

heated at  $10 \text{ K}\cdot\text{min}^{-1}$  under flowing helium ( $0.044 \text{ mol}\cdot\text{s}^{-1}$ ) at reduced pressure (13.3 kPa), and the desorbed ammonia was detected by mass spectrometer (ULVAC UPM-ST-200 or ANELVA M-QA 100 F). After the measurement, the peak intensity was calibrated using a known amount of ammonia.

EPR spectra were measured with a Jeol Jes-Re3x spectrometer (JEOL Co., Ltd., Tokyo, Japan) equipped with a PC using Esprit-425 software for the spectrometer control and data acquisition at X-band (9.0 GHz), at a power of 1 mW and modulation frequency of 100 KHz. The spectra were measured at 300 and 77 K. The sample charges were around 20 mg placed in EPR-grade quartz tubes with i. d. of 2 mm. The  $g$  values were determined in comparison with a small signal of the standard DPPH ( $g = 2.0036$ ). Experimental EPR spectra were also simulated with the Esprit-425 Jeol software, which uses a second-order perturbation theory for the determination of the axial and rhombic  $A$  and  $g$  hyperfine parameters and the wide  $\sigma$  of associated absorption-like Gaussian lines. This program does not include the broadening effects of strains.

Throughout the text and figures, samples are abbreviated as HMor for the initial protonated form of mordenite, and Cu-Mor for Cu-exchanged forms, followed by the MR value and temperature of hydrogen reduction in  $^{\circ}\text{C}$ , if applicable (*e.g.*, CuMor15-250).

### 3. Results and discussion

#### 3.1. Characterization of H-mordenites

A set of mordenites, including deeply dealuminated ones with MR values, ranging to 206 were used in this study. Assuming that the crystal structure could be significantly influenced during this treatment, crystallinity of the samples was tested. XRD patterns for the set of HMor with varying MR are shown in Fig. 1. The unit cell parameters obtained from the experimental spectra by Rietveld refinement for HMor, and reference data for NaMor from IZA Structure Commission [11] are shown in Table I. Parameters “ $a$ ” and “ $c$ ” were less affected, while “ $b$ ” changed significantly in comparison with the reference data. There were no significant differences in the values of “ $a$ ”, “ $b$ ” and “ $c$ ” for the series of HMor samples. Reduction of the parameter “ $b$ ” led to a small decrease in channel aperture, and to an increase in its elliptical cross-section aspect ratio, since the parameter “ $a$ ” varied less. The

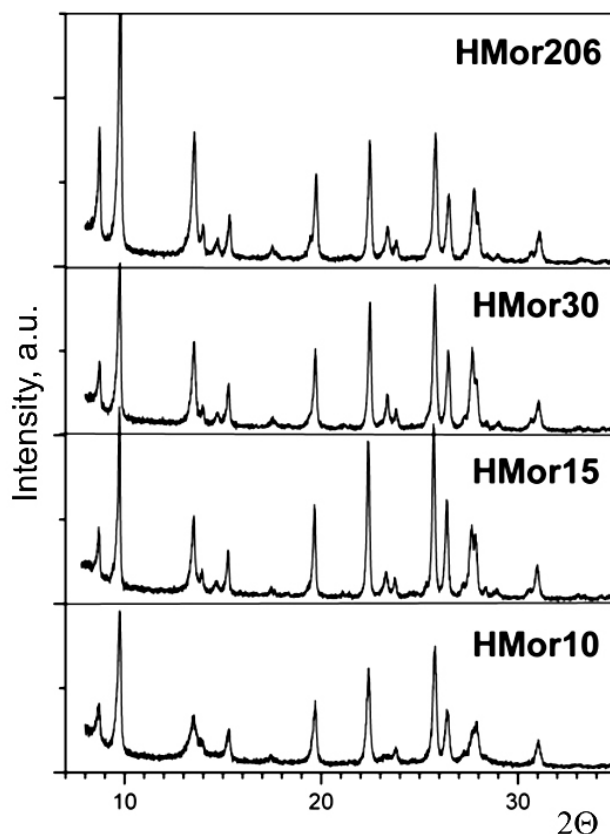


FIGURE 1. XRD patterns of the set of protonated mordenites.

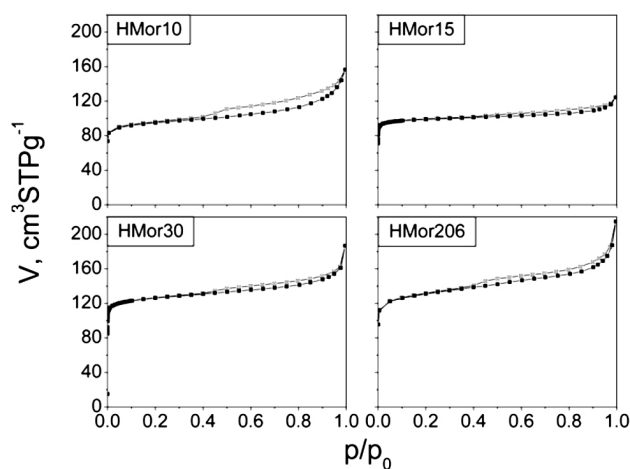


FIGURE 2. Isotherms of  $\text{N}_2$  adsorption of the HMor set.

change in the “ $c$ ” parameter evidences, that the lattice became slightly denser in [001]-direction. Variation of XRD patterns of H-mordenites was observed with increasing MR. Thus, several reflections in the range of  $2\theta=13\text{--}18^{\circ}$  changed their appearance and relative intensities, as did doublets at  $23\text{--}24^{\circ}$  and  $28^{\circ}$ . Remarkably, in spite of the variation in XRD patterns, a systematic dependence of the lattice parameters on MR cannot be inferred. Detailed discussion and refinement of crystalline structure of this mordenite series is beyond the scope of the present work and will be reported elsewhere.

TABLE I. Lattice parameters for mordenites.

Sample	$a$ , Å	$b$ , Å	$c$ , Å
NaMor [10]	18.11	20.53	7.528
HMor10	18.04	20.29	7.465
HMor15	18.15	20.29	7.487
HMor30	18.14	20.25	7.470
HMor206	18.07	20.27	7.470

TABLE II. Characteristics of HMor porosity and copper content measurements

	HMor10	HMor15	HMor30	HMor206
$S_{BET}$ , m <sup>2</sup> /g	359	380	480	493
$S_t$ , (external surface) m <sup>2</sup> /g	45	33	51	68
$V_{\Sigma}$ , cm <sup>3</sup> /g	0.200	0.174	0.238	0.261
Mesopore volume, cm <sup>3</sup> /g (Pore radii 2-50 nm)	0.07	0.05	0.06	0.05
Al concentration derived from MR, mol/kg	2.56	1.83	1.01	0.16
TPD-derived conc. of acid sites, mol/kg	0.44	1.24	0.49	0.13
Copper content after ion exchange, wt %	0.79	0.26	0.26	0.44
Maximum (theoretical) ion-exchange capacity on the basis of MR, with respect to Cu <sup>2+</sup> , wt % of Cu	8.2	5.9	3.2	0.5
% of ion exchange	9.6	4.4	8.1	86.3

The most important conclusion for the discussion of this paper is that sample crystallinity was not affected by the dealumination treatment and neither the degradation of the crystalline pattern nor appearance of an amorphous phase was observed.

The results of HMor porosity characterization and copper content measurements are presented in Table II. The  $S_{BET}$  value increased with MR growth; a maximum increment occurred in the passage from HMor15 to HMor30. Meanwhile, the total pore volume  $V_{\Sigma}$  reached a minimum for HMor15. It is important to note that in the case of ideal mordenite crystals possessing regular channels with elliptical cross-section 0.65×0.70 nm, the material had a micropore volume equal to 0.14 cm<sup>3</sup>/g [10]. Reduction of the “*b*” and “*c*” parameters (Table I) can lead to a decrease in this volume of not more than ~1%. The higher values of the observed micropore volume refer to perfect mordenite crystal, and the mesopore volume (with non-structural radii of up to 50 nm) can be associated with defects in the microcrystals, probably originating from the synthesis conditions employed by the manufacturer, TOSOH Corporation of Japan (*not reported*). These provide the additional contribution to  $V_Z$  due to irregular porosity inside the crystal volume.

Variation of the total observed surface area showed that the microstructure of these matrices depends on MR, although the crystal structure only showed a subtle variation with MR (Fig. 1). Some correlation of the data on the total surface area and pore volumes exists, and the least “porous” HMor15 was characterized by the lowest values of mesopore volume. The mesopores can be associated with cleaved areas of microcrystals, defects, uneven surface, etc., and seem to be nearly independent from the amount of Si substituted by Al in the ideal tetrahedral TO<sub>4</sub> coordination. Meanwhile, according to these data, the HMor15 showed the minimum concentration of defects and other above-mentioned structure features providing the increase in porosity. Thus, HMor15 is expected to have the least amount of defects of crystal structure in the given series. This may be a reason of the further

featured behavior of copper ions after incorporation and reduction in this mordenite.

Isotherms of N<sub>2</sub> adsorption at 76 K (Fig. 2) confirm these conclusions. The HMor15 sample, unlike the other mordenites, exhibits a saturation zone in the interval of 0.1 <  $p/p_0$  < 0.8 indicating that the micropores are homogeneous, and only a mild increase in the capacity of adsorption for  $p/p_0 > 0.9$  was observed. For the samples HMor30 and HMor206 the cycles of hysteresis type III [25] were better defined, being highest for HMor10, and indicating the greater contribution of mesopores in these samples.

Complete exchange of 2H<sup>+</sup> ions in HMor for Cu<sup>2+</sup> ion leads to the composition Cu<sub>*x*</sub><sup>2+</sup>Al<sub>2*x*</sub>Si<sub>*y*</sub>O<sub>96</sub>, where  $y/x=MR$ ; the amount of copper is expected to change definitely with a change in MR. Copper content was measured for ion exchanged samples and the degree of the ion exchange was calculated (Table II). Experimental results demonstrate that not all the samples attained the complete exchange in spite of the long contact (a day) of zeolite samples with the solution in which the amount of Cu<sup>2+</sup> ion was in large excess. Samples HMor10, HMor15 and HMor30 were far away from completion of the ion-exchange (Table II), and only HMor206 approximated it to ~86%. That is, almost all acid sites in HMor206 participate in the copper incorporation, while in the other samples only few of the sites are active in this process. In fact, less than 10% of total occupancy is attained for HMor10, HMor15, and HMor30, and Cu<sup>2+</sup> ions are expected to occupy the more energetically favorable centers in these mordenites. The lowest degree of exchange with respect to copper ions occurred in the HMor15 sample, the next larger being in HMor10. Such dependence of copper ion-exchangeability vs. MR, with an extreme lying within the MR range, can be associated with appearance only in the HMor10 samples extra-framework Al atoms in 5-coordinated state. This Al moiety has been characterized by <sup>27</sup>Al MAS-NMR [26] and shows the chemical shift  $\delta = 27$  ppm (essentially different from the value for the tetrahedrally coordinated framework Al atoms,  $\delta = 57$  ppm [27]). Also,

all samples contain some amount of extra-framework octahedrally coordinated Al atoms; these form additional active Lewis sites with  $\delta \sim 0$  ppm and can incorporate more  $\text{Cu}^{2+}$  ions [26].

Thus, the regular MR increase of mordenite samples did not result in a variation of the amount of exchangeable cations only. Much more difference was observed in structure disorder both at the levels of micro- and meso-structure of these zeolites (Table II). Not only ion-exchangeability, but also other properties showed an extreme for HMor15.

Acid properties of H-mordenites with  $10 \leq \text{MR} \leq 206$  were investigated by IR-spectroscopy [16] with adsorption of probe molecules (CO and pyridine). It has been established that concentration and strength of both Lewis and Brønsted sites depend on MR in a complicated way. Two types of Brønsted acid sites with corresponding IR bands,  $\nu_{\text{OH}} = 3610$  and  $\nu_{\text{OH}} = 3720 \text{ cm}^{-1}$ , were observed, their concentration reaching a maximum for intermediate MR. Also, H-mordenites possess four types of Lewis acid sites. Their concentration is minimal for mordenites with intermediate MR, and it increases for higher and lower MR [16].

In the present work we studied the acid properties of the selected mordenites in greater detail. Fig. 3 shows the results of the ammonia TPD study. The measurements argue for a significant difference between the mordenites used, and a non-monotonic dependence of the TPD pattern is observed with increasing MR. There are at least three main maxima at the TPD curves in Fig. 3, the relative contribution of which varied with MR. The lowest-temperature peak, ca. 490 K, which dominates for the HMor10 sample, belongs to the weakly bonded ammonia probably adsorbed on extra-framework Lewis sites. Intensity of this peak falls with increasing MR. The TPD curve for HMor10 also shows a shoulder from which a maximum at ca. 660 K can be resolved. The well-pronounced maximum at ca. 730 K occurs for the other three mordenites with little shift to the lower temperatures while changing from HMor15 to HMor206.

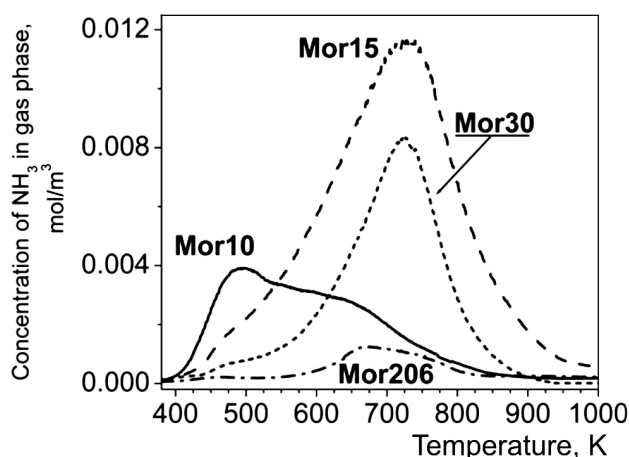


FIGURE 3. Ammonia TPD spectra of HMor samples.

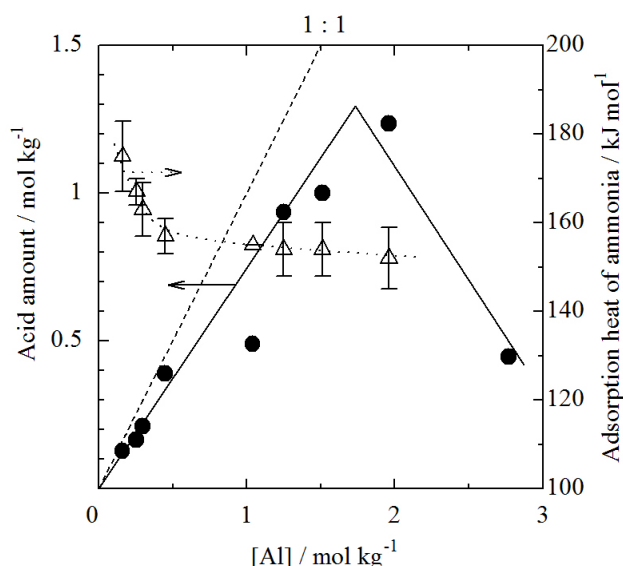


FIGURE 4. Amount and strength of acid sites on H-mordenite with various aluminum concentrations. Values for mordenites with intermediate MR (not applied in this work) are shown also. MR values for filled circles (right to left) are 10, 15, 20, 24, 30, 72, 110, 128 and 206 respectively.

These maxima are not symmetrical, and evident contributions from some species developing a desorption peak at 660 K can be evaluated.

The above three ammonia thermodesorption peaks, 450–490 (very likely Lewis), 660 and 730 K (Brønsted), are associated with the three different groups of acid sites, the amount of which is very variable for different MR. On the basis of the above-mentioned NMR data on the existence of the extra-framework pentacoordinated Al in HMor10, accompanied by the growth of ion-exchangeability with respect to copper ions, we may suppose that these unusual Al atoms are responsible for the acid properties with the lowest strength, resulting in the 450–490 K peak. Note also that, for the HMor15 sample, some amount of ammonia is desorbed even at temperatures  $\geq 900$  K, so a population of extremely strong acid sites probably exists for this sample and is absent for the other three mordenites.

The amount of acid sites was calculated from the intensity of  $\text{NH}_3$  desorption peaks, and plotted against the aluminum concentration in Fig. 4, solid line. From the point of view of zeolite structure the ratio of  $[\text{Al}]:[\text{OH}]$  must be 1:1 (Fig. 4, dashed line). Experimentally determined concentration of acid sites is slightly lower than the theoretically expected concentration in the range from 0.1 to  $\sim 1.5 \text{ mol kg}^{-1}$ , and decreases with further increase in aluminum content. The maximum deviation is observed for HMor10. As previously reported [28], at aluminum concentration higher than  $1.5 \text{ mol kg}^{-1}$ , destruction of the crystal structure of H-mordenite is induced by humidity, resulting in the generation of Lewis acidity (TPD peak at 490 K, Fig. 3).

The acid strength was calculated by the curve-fitting method as ammonia adsorption heat (Fig. 4). The acid

TABLE IV. Specific concentration and pK<sub>a</sub> of Brønsted acid sites for the set of mordenites.

HMor10		HMor15		HMor30		HMor206	
BAS pK <sub>a</sub>	C <sub>BAS</sub> , μmol/m <sup>2</sup>	BAS pK <sub>a</sub>	C <sub>BAS</sub> , μmol/m <sup>2</sup>	BAS pK <sub>a</sub>	C <sub>BAS</sub> , μmol/m <sup>2</sup>	BAS pK <sub>a</sub>	C <sub>BAS</sub> , μmol/m <sup>2</sup>
		1.5	0.92			1.5	0.32
		2.0	1.00	1.8	0.50	1.8	0.34
2.8	0.18	2.3	0.76	2.9	0.92	2.4	0.36
3.9	0.22			3.4	0.52	3.3	0.24
5.0	0.84	5.5	0.18	5.0	0.20	4.0	0.06
5.7	0.24	6.1	0.28	5.6	0.10	5.4	0.06

strength starts from ca. 180 kJ·mol<sup>-1</sup> for HMor206. With increasing aluminum content acid strength falls in the range of 0.1-0.5 mol·kg<sup>-1</sup>, and finally in the range of 0.5-2 mol·kg<sup>-1</sup> reaches a constant value, ca. 150 kJ·mol<sup>-1</sup>, and becomes independent of aluminum concentration, in agreement with Katada *et al.* [23]. The TPD curve for the HMor10 sample manifests a bimodal distribution of acid sites, and it is hard to define a mean value of their acid strength by this method. The point corresponding to HMor10 sample in Fig. 4 is marked for the high-temperature shoulder at ca. 660 K.

The extra-framework Al is expected to form less acid hydroxyl than other aluminum atoms in zeolites. On the other hand, the main peak, 730 K, corresponds to the acid sites with the highest concentration for HMor15 and HMor30. Its amount in HMor15 is ~2.5 times higher (Fig. 4) compared with HMor30, which approximately correlates with their MR values. However, comparing these amounts with that of HMor10, the increase of Al concentration resulted in a significant fall in the total amount of acid sites. The increase in copper concentration in the CuMor10 and CuMor206 samples compared with the CuMor15 and CuMor30 samples cannot be explained by the additional involvement of active sites formed with the extra-framework Al since the total amount of acid sites does not grow in these cases. Thus, we propose that copper incorporation and ammonia bonding do not show a unique quantitative correspondence, and hence, affinity of the protonated forms of mordenite with respect to Cu<sup>2+</sup> is controlled in a more complicated way than indicated by the acid-base ammonia interaction.

In the case of the HMor206 sample, the TPD curve showed a peak at 660 K, similar to that for HMor10 and a high temperature peak at 730 K. Thus, the HMor206 sample should have the rather high strength of acid sites (which coincides with the high average adsorption heat of ammonia, Fig. 4), but with low total amount.

As the ammonia TPD curve shows the results of the whole set of acid sites integrated in a sample, it was of interest to detect individual acid sites with different strength. Surface concentration of nonequivalent Brønsted acid sites (BAS) with different pK<sub>a</sub> was determined by non-aqueous titration. Results are listed in Table III. All samples have a number of different types of BAS in a wide range of pK<sub>a</sub>.

The HMor10 sample showed four types of BAS with weak and moderate strength (2.8 < pK<sub>a</sub> < 5.7) that correlated with the TPD data mentioned above. A large quantity of strong BAS (1.5 < pK<sub>a</sub> < 2.3) was present in HMor15, although some amount of sites of weak and medium strength (5.5 < pK<sub>a</sub> < 6.1) were present on its surface in smaller amounts. It is worthy of note that HMor15 also showed the weakest acid sites with pK<sub>a</sub>=6.1, in line with the high concentration of the BAS with the most acid properties (pK<sub>a</sub>=1.5). The same BAS with pK<sub>a</sub>=1.5 were present at HMor206 in relatively high concentration, while very low amounts of other types of BAS with pK<sub>a</sub> > 3.3 were present on the surface of this sample. Such distribution of acid sites concentration can explain the high integrated heat of ammonia desorption for HMor206.

### 3.2. EPR of H-mordenites and Cu-exchanged mordenites

EPR spectroscopy was employed to characterize the set of hydrated HMor and CuMor with varying MR. In the case of the set of hydrated HMor series, only HMor-10 present a weak absorption at g=4.3, which can be assigned to tetrahedral Fe<sup>3+</sup> impurities, substituting for tetrahedral silica (Fig. 5, curve a). No EPR signal was observed at 300 K for other HMor samples for low and high fields up to 600 mT (Fig. 5). The EPR radical signal at g = 2.0036 of Fig. 5 comes from the DPPH marker.

The EPR spectrum of hydrated CuMor10 (Fig. 6a) shows a resolved low field hyperfine interaction site, site H1, in its hydrated ERP spectrum at room temperature; see Fig. 6a, and Table 4. The setting of this hyperfine interaction H1, reflects certain degree of immobilization of the Cu<sup>2+</sup> cations possibly due to the coordination with network oxygen. The room temperature EPR spectra of hydrated CuMor15 (Fig. 7a), CuMor30 (Fig. 8a) and CuMor206 (Fig. 9a) are broad and structureless, with isotropic absorptions at g<sub>eff</sub> = 2.148, 2.148 and 2.148, respectively, indicating typical motional broadening, that is, mobility of hydrated Cu<sup>2+</sup> complex such as Cu(H<sub>2</sub>O)<sub>6</sub><sup>2+</sup> in mordenite channels with bonding characteristics similar to those of Cu(H<sub>2</sub>O)<sub>6</sub><sup>2+</sup> in solution, commonly observed in hydrated Cu-exchanged zeolites [29,30].

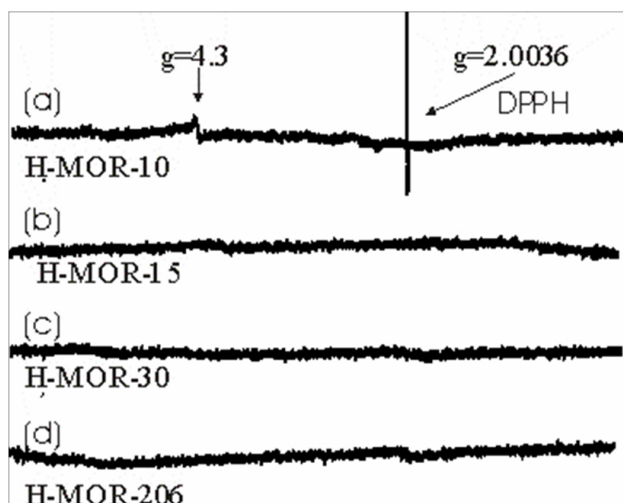


FIGURE 5. EPR spectra of hydrated: a) HMor10, b) HMor15, c) HMor30 and d) HMor206, measured at 300 K.

### CuMor10

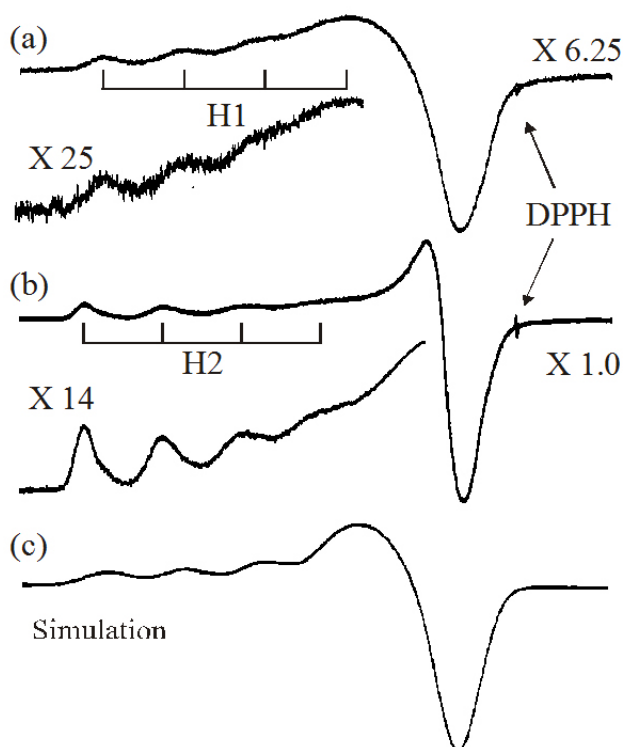


FIGURE 6. EPR spectra of CuMor10. a) Measured at 300 K. b) Measured at 77 K. c) simulated EPR rhombic spectra of hydrated CuMor10 measured at 300 K, the EPR parameters of this simulation are shown in Table IV.

The liquid nitrogen temperature EPR spectra of the hydrated samples show the resolved low field features, belonging to slightly different sites H2, H3 and H4 for CuMor10, CuMor15 and CuMor30 respectively (Figs. 6b, 7b, 8b and Table IV). These hyperfine low field features are due to the freezing of motional effects, and are commonly observed in

hydrated Cu-exchanged zeolites below 120 K [30,31]. Only the hydrated CuMor206 sample presents two hyperfine sites H5 and H6 at 77 K. The four hyperfine lines in the low field region come from the coupling to the copper nucleus with  $I=3/2$ .

The experimental amplification of the low hyperfine region is shown below the each EPR spectra, characterized by the four absorption-like lines showing a spectral broadening increase from low to high fields, attributed to correlated g- and A-strain effects [31,32]. This broadening dependence is not observed in the four absorption-like lines of the EPR of CuMor10 at 300 K (see EPR amplification of Fig. 6a).

The best EPR rhombic and axial hyperfine values at 300 and 77 K of paramagnetic  $\text{Cu}^{2+}$  ions of the CuMor set, obtained by simulation (Table IV) have been attributed to motional freezing of hydrated  $\text{Cu}^{2+}$  complex in octahedral sites.

Listed in the Table IV simulated hyperfine EPR parameters for sample CuMor10 at 300 K are assigned to a rhombic site with  $g_{zz} = 2.362$ ,  $g_{xx} = 2.135$  and  $g_{yy} = 2.077$ . The spectrum and its simulation (see Fig. 6c) show that  $\text{Cu}^{2+}$  ions in CuMor10 present hyperfine features without strained effects. This fact can be related to the lack of mobility of hydrated  $\text{Cu}^{2+}$  complex [33], probably due to complex bonding to the mordenite lattice [31].

The obtained hyperfine values of hydrated CuMor10, CuMor15 and CuMor30 samples at 77 K have been simulated

### CuMor15

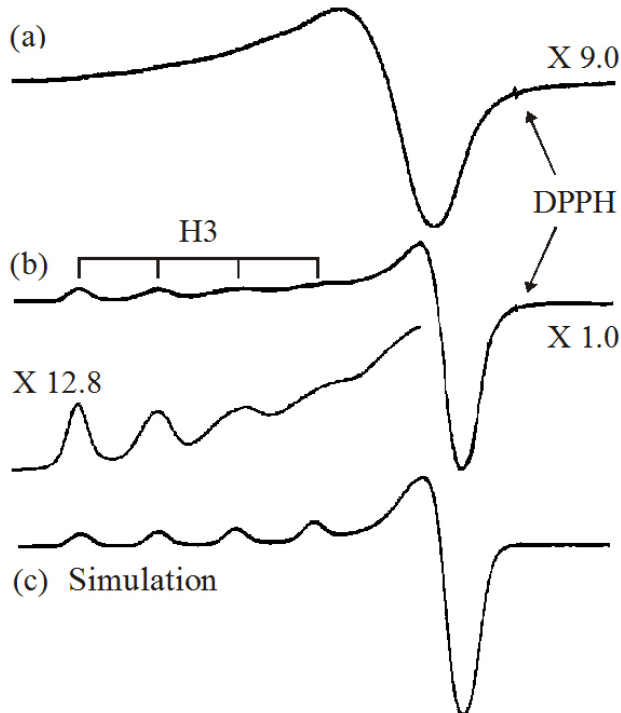


FIGURE 7. EPR spectra of CuMor15. a) Measured at 300 K. b) Measured at 77 K. c) Simulated EPR rhombic spectra of hydrated CuMor15 measured at 77 K, the EPR parameters of this simulation are shown in Table IV.

TABLE IV. EPR parameters for hydrated Cu-Exchanged mordenites.

Sample	Site	$g_{zz}(g_{  })$	$g_{xx}(g_{\perp})$	$g_{yy}$	$A_{zz}(A_{  })$ (mT)	$A_{xx}(A_{\perp})$ (mT)	$A_{yy}$ (mT)	$\sigma_{zz}(\sigma_{  })$ (mT)	$\sigma_{xx}(\sigma_{\perp})$ (mT)	$\sigma_{yy}$ (mT)	Relative intensity <sup>a</sup>
CuMor10	H1 <sup>b</sup>	2.362	2.135	2.077	13.0	1.5	0.0	7.7	10.5	5.8	0.09
	H2	2.388	2.094	2.072	13.3	0.45	0.0	3.7	5.3	3.0	0.40
CuMor15	H3	2.400	2.097	2.073	12.9	0.05	0.0	3.5	5.7	2.9	1.00
CuMor30	H4	2.401	2.096	2.076	13.0	0.02	0.0	3.5	6.9	3.0	0.68
CuMor206	H5	2.410	2.080	-	12.0	-	0.0	-	-	-	-
	H6	2.373	2.080	-	14.1	-	0.0	-	-	-	0.15

Estimated errors  $g_s = \pm 0.003$ ,  $A_s = \pm 0.2$  mT,  $\sigma_s = \pm 0.2$  mT, the sub-indices  $s$  means the tensor components  $x$ ,  $y$  and  $z$  of each EPR parameter.

<sup>a</sup>Estimated errors in relative intensity = 0.15.

<sup>b</sup>EPR parameters for spectrum measured at 300 K, all other EPR parameters belong to spectra measured at 77 K.

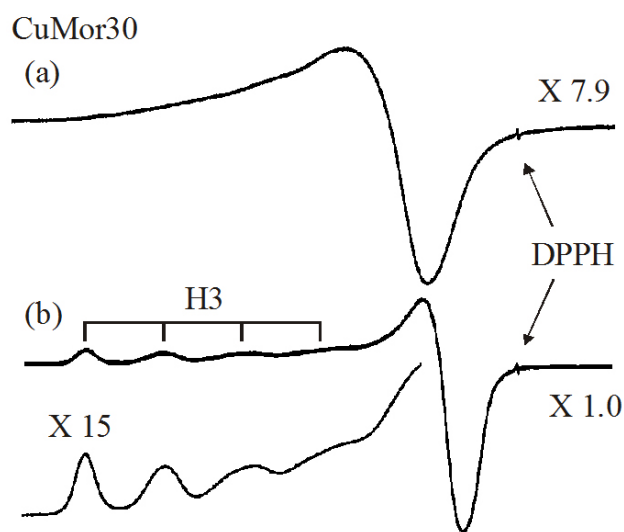


FIGURE 8. EPR spectra of CuMor30. a) Measured at 300 K. b) Measured at 77 K.

as an axial site with  $g_{zz} = 2.388$ , 2.400 and 2.401,  $g_{xx} = 2.094$ , 2.097 and 2.096 and  $g_{yy} = 2.072$ , 2.073 and 2.076, respectively, shown in table IV. Finally, the EPR simulation of hydrated CuMor206 sample at 77 K has been carried out only for the  $g_{zz}(g_{||})$  region with two axial sites, one with  $g_{||} = 2.410$  and the second axial site with  $g_{||} = 2.373$ .

Homogeneity of the copper state at 77 K in the samples CuMor10, CuMor15 and CuMor30 demonstrates, that at low Cu exchange levels (less than 10 %, see Table II) copper ion in these samples occupies the only one possible site. The second site begins to be populated only in the case of CuMor206, with 86% Cu ion exchange (Table II).

In the last column of the Table IV, it is the EPR intensity of the Cu<sup>2+</sup>-EPR signals of the CuMor set, normalized to the intensity of the CuMor15 sample. This intensity is calculated from the area of EPR adsorption as the second integral of the measured EPR spectra and is proportional to the number of resonant items in each sample. The founded intensity values for CuMor10, CuMor15, CuMor30 and CuMor206 samples

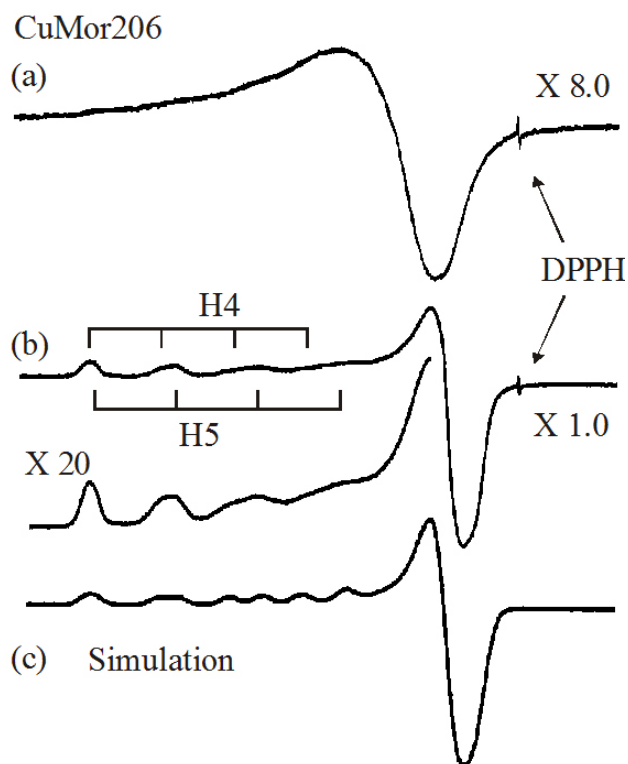


FIGURE 9. EPR spectra of CuMor206. a) Measured at 300 K. b) Measured at 77 K. c) Simulation of two axial sites of hydrated CuMor206 spectra measured at 77 K, the EPR parameters of this simulation are shown in Table IV.

are 0.40, 1.00, 0.68 and 0.15, respectively. These relative intensities are plotted as a bar graph in Fig. 10 and it is shown that the amount of Cu<sup>2+</sup> ions follows the order CuMor15 > CuMor30 > CuMor10 > CuMor206. As we have observed in resent studies about copper reduction in Cu exchanged in Cu-Erionite [34] and in Cu-ZSM5 [35], one of the precursors of metallic copper formed under reduction upon hydrogen atmosphere are the Cu<sup>2+</sup> ion observed by EPR. In the case of Cu-Erionite we have found that the intensity of the broad and structureless ERP signal at room temperature

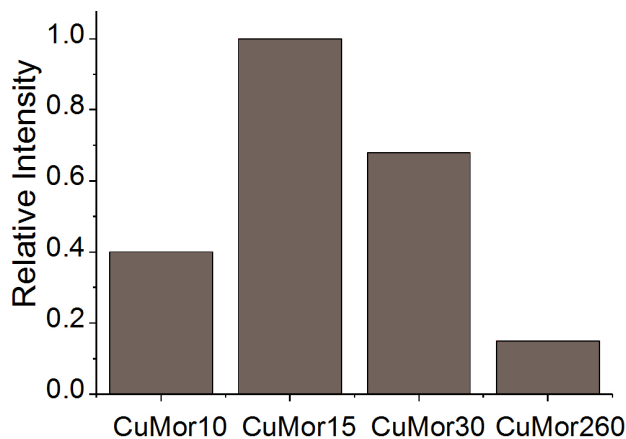


FIGURE 10. Bar graph of the relative intensities (second derivative of the EPR signal) for the set of CuMor samples. Intensities normalized to sample CuMor15.

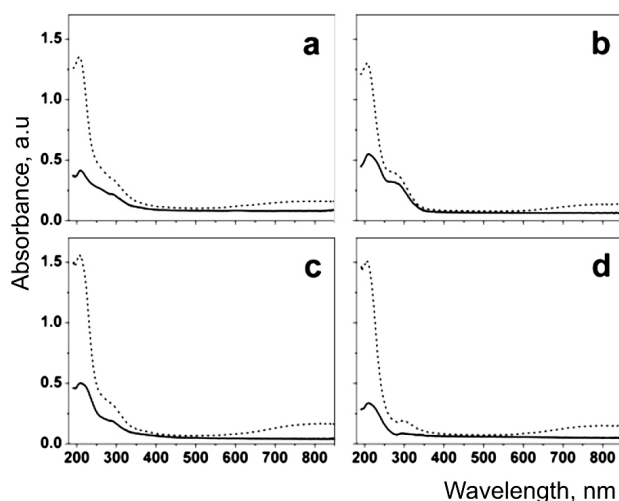


FIGURE 11. Absorption spectra of H-mordenites (solid lines) and their Cu-exchanged forms (dotted lines) with MR 10 (a), 15 (b), 30 (c) and 206 (d).

decreases as the temperature of the reduction treatment increases, then the copper EPR intensity can be used to monitor the changes in  $\text{Cu}^{2+}$  population in a reduction process, an ERP study over the CuMor series under reduction conditions is actually in progress.

### 3.3. DRS of Cu-exchanged mordenites

The absorption spectra of the initial HMor and of the CuMor samples prepared by ion exchange are shown in Fig. 11, a-d. The mordenite matrix without copper showed the expected absorption in the range  $\lambda < 350$  nm. A clear maximum at  $\sim 210$  nm was observed for all mordenites under study. Other less expressed features showed different appearances in the samples: HMor10 had a weak feature at about 300 nm, which was transformed into the shoulders for HMor15 and HMor30 samples, while HMor206 showed practically no absorption at range  $\lambda > 280$  nm. The absorption bands in this short-wavelength range are inherent to zeolites of different types,

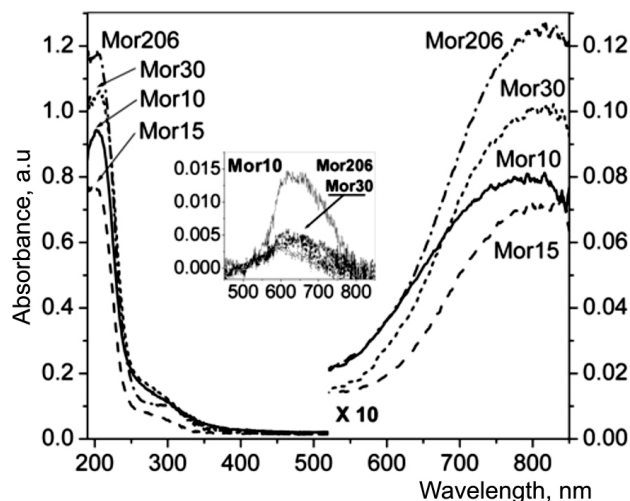


FIGURE 12. Subtractive absorption spectra, showing the copper contribution in CuMor spectra. Inset displays the differential absorption at  $\lambda=620$  nm for the sample CuMor10 ( $\Delta=D(\text{CuMor10})-D(\text{CuMor15})$ ) and much weaker ones for CuMor30 and CuMor206 samples.

and they can originate from the charge transfer  $\text{O}^{2-} \rightarrow \text{Al}^{3+}$  with participation of aluminum atoms at specific locations (surface, corners, defects, etc.) [36].

The incorporation of copper led to the appearance of an intensive band at  $\sim 208$  nm for all CuMor samples. This band corresponds to the ligand-to-metal charge transfer transition from oxygen to  $\text{Cu}^{2+}$  [37]. Simultaneously, a weak band with a maximum at  $\sim 810$  nm appeared (Fig. 11). This band is typical for spin-allowed  $d-d$  transition  ${}^2E_g \rightarrow {}^2T_{2g}$  of  $\text{Cu}^{2+}$  ion in pseudo-octahedral oxygen coordination, e.g.  $\text{Cu}(\text{H}_2\text{O})_6^{2+}$  [37,38] and  $\text{Cu}^{2+}$  in solid  $\text{Al}_2\text{O}_3$  matrix [39]. Differences in the spectra of CuMor and HMor allowed us to extract the proper copper absorption in the CuMor spectra (Fig. 12). Outlines of  $d-d$  bands for differential CuMor spectra are in general the same; the shape of this band is somewhat dissimilar only for CuMor10. This appearance of the band of  $\text{Cu}^{2+}$   $d-d$  transitions can provide qualitative information on the state of copper ions, as the acid properties of different mordenites may influence their surrounding coordination. The main part of the six oxygen ligands in the first coordination shell of  $\text{Cu}^{2+}$  belongs to water molecules, but a variable minor part of them is from the zeolite framework. The number of framework oxygen atoms included in the coordination shell must depend on the properties of mordenite and on the different treatments applied to the sample. For the freshly prepared samples the experimental maxima of  $d-d$  transitions are shifted in the range 810-830 nm (Fig. 12). Blue shift of this band in comparison with  $\sim 900$  nm for  $\text{Cu}(\text{H}_2\text{O})_6^{2+}$  ion in aqueous solutions indicates the increase of ligand field while the water molecule is replaced by framework oxygen. Short-wavelength slope of the  $d-d$  bands of CuMor30 and CuMor206 samples shows a very weak band at  $\sim 620$  nm, which is absent in the spectrum of the CuMor15 sample. So, differences in the spectra of other samples compared to the

CuMor15 spectrum allows to extract the band at  $\sim 620$  nm (Fig. 12, inset). This band shows the highest intensity in the spectrum of the CuMor10 sample. The state of Cu<sup>2+</sup> with band at 620 nm corresponds to the distorted complexes, like the square pyramidal or square planar complexes [40], extreme cases of tetragonal distortion of the oxygen octahedron due to the Jahn-Teller effect [41]. Thus, at least two states of Cu<sup>2+</sup>, differing in coordination polyhedra are presented in the samples CuMor10, CuMor30 and CuMor206 (Fig. 12, inset). Their appearance testifies to the difference in interaction of the ions with mordenites depending on MR.

### 3.4. DRS of reduced Cu-mordenites

The DRS data of the reduced samples contain many new features. Under reduction conditions the d-d band starts to disappear, which indicates a degree of completeness of the reduction. The mordenite samples reduced in temperatures from 150 to 450°C reveal that four new features that appear in the spectra as well as strong changes in the two bands associated with Cu<sup>2+</sup> cited in the previous paragraph ( $\sim 810$ -830 nm and 208 nm). Altogether, the following six features are seen in spectra, as shown by arrows in Figs. 13-16:

- (i) the charge transfer band of Cu<sup>2+</sup> at  $\sim 210$  nm;
- (ii) the small maximum at  $\sim 250$  nm;
- (iii) the feature at 300-350 nm;
- (iv) the feature at 400-500 nm;
- (v) the band peaking at 550-600 nm with complex dependence on the line shape while MR is changing;
- (vi) the band of d-d transition of Cu<sup>2+</sup> at  $\sim 810$ -830 nm.

The maximum (i) of the charge transfer band diminished with temperature increase. This temperature dependence allows the assumption that the reduction process is not complete at 150°C but goes on up to 450°C. Overlapping of this band with the proper absorption of the mordenite matrix itself complicates an unambiguous attribution of this peak, especially in the case of its low intensity. Some small copper clusters can also be proposed as species responsible for the absorption in this region [21]. The charge transfer band certainly makes a contribution to absorbance with a maximum at  $\sim 210$  nm, as long as the d-d band of Cu<sup>2+</sup> (vi) is simultaneously present in the spectra.

The weak band (ii) at 250 nm coincides with a band of isolated or poorly associated Cu<sup>+</sup> ions [42]. In general, in contrast with the peaks (i) and (vi), as temperature rose, the intensity of this absorption band (ii) was higher.

Features (iii), (iv) and (v) at 300-350 nm, 400-500 nm and 550-600 nm respectively can be discussed together as belonging to the reduced Cu(0) products (copper nanoparticles in the size range  $< 10$  nm) interpreted earlier in more detail in [22]. The less pronounced but insistent bands (iii) and (iv)

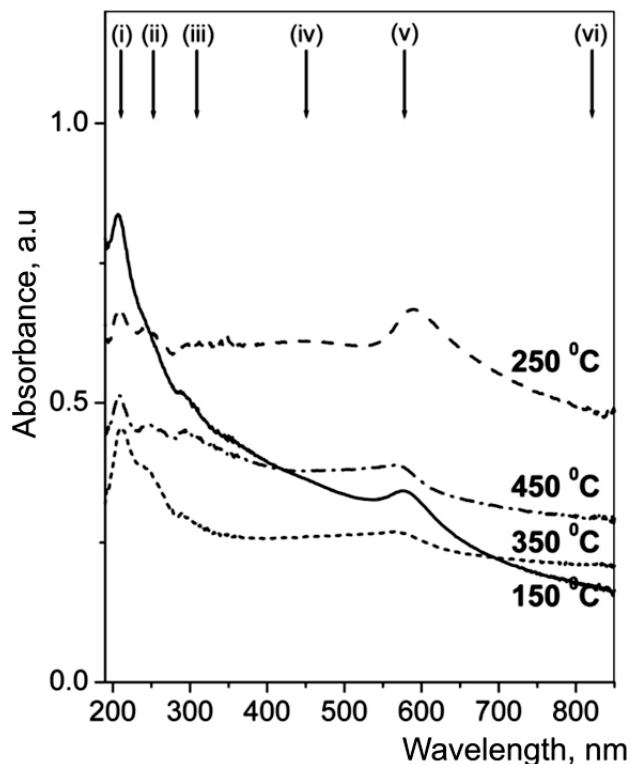


FIGURE 13. Absorption spectra of CuMor10 reduced at different temperatures.

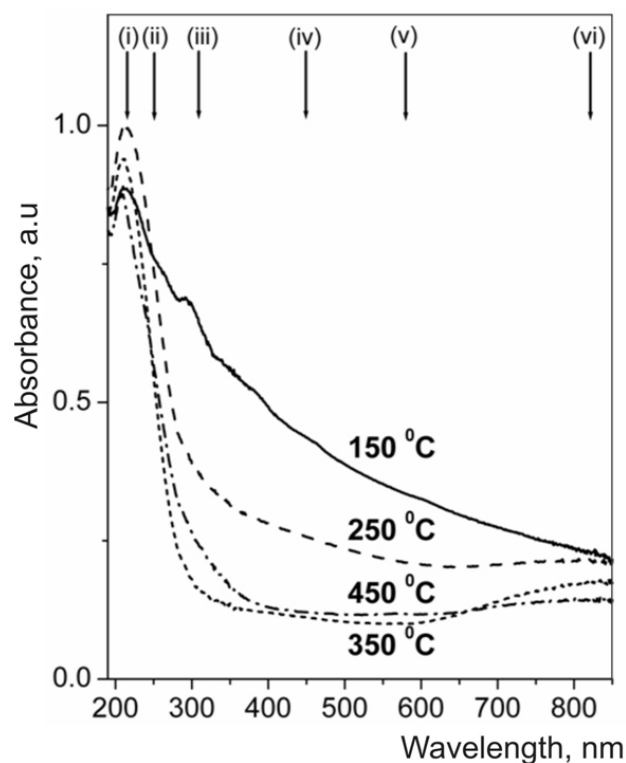


FIGURE 14. Absorption spectra of CuMor15 reduced at different temperatures.

appear in line with the main maximum (v), usually with increasing temperature. It is known that the spectrum of copper

nanoparticles includes additional structure together with the classical Mie-theory plasmon resonance due to features of the copper band structure.

The band (v) at  $\lambda=550\text{-}600$  nm appears and increases with temperature for all mordenites (Figs. 13, 15, 16) except for CuMor15 (Fig. 14). Temperature of appearance and shape of this feature strongly depend on MR. It comes off in the peak for reduced CuMor10-150, CuMor10-250 (Fig. 13) and CuMor206-350, CuMor206-450 (Fig. 16) samples, or as a step-like shoulder in the same range of wavelengths for CuMor30 starting from 250°C (Fig. 15). It is of interest to note that starting from the peak at low temperatures it changes to a shoulder at higher temperatures only in the case of CuMor10 samples (Fig. 13). The shape of this feature for CuMor30 - CuMor206 samples does not depend on the temperature of reduction, but its intensity (either peak or shoulder) varies significantly (Fig. 15 and 16).

Simulation of the same spectral features (iii-v) for copper nanoparticles based on the familiar relations from the Mie theory allowed us to conclude [22] that size of the particles and the medium dielectric function  $\epsilon_0$  significantly affect their intensity and shape, while the position of the band is much less affected. The larger size of particles results in the higher intensity of the plasmon resonance (v). The increase of  $\epsilon_0$  also has an absorption-enhancing effect. The shoulder in the range 550-600 nm can be attributed to small copper particles located predominantly at the outer surface of mordenite microcrystals. The pronounced maximum at the same range may be due to larger copper particles and to a higher dielectric function of the medium. Since plasmon band appears for the particles larger in size than regular mordenite channels of  $\sim 0.7$  nm diameter, the copper particles can be formed inside mesopores existing in mordenite crystals. These could be cleaved areas in which the mordenite matrix surrounds a copper particle. In fact, the mordenites used in this work have porosity at different levels (Table II). It is worth to note that the use of non-crystallographic pores in crystals is currently considered as a new approach in catalyst design [43,44].

Thus, the spectra in Figs. 13-16 evidence that formation of the larger particles is more favorable in CuMor10 and CuMor206 and less favorable in CuMor30. In spite of the non-monotonic variation of this phenomenon vs. MR, this fact correlates with the rise in porosity and the decrease in acidity of mordenite. The highest acidity of HMor15 leads to the less favorable conditions for copper reduction and complete absence of the plasmon resonance band (v).

In line with the above-mentioned bands, other features like an increase in background absorption (Fig. 13, 16), or a broad descent in absorption from the UV region to the end of the available range (Fig. 13) may be seen in the spectra. Their appearance, as well as the development of the all aforementioned peaks to their full extent depends on MR (Figs. 13-16), and we consider them separately for different mordenites.

### 3.4.1. DRS of the reduced CuMor10

Peak intensity (i) significantly decreased with increasing reduction temperature; absorbance at this wavelength returned to the absorbance of the HMor10 sample (Fig. 13 and Fig. 11). Simultaneously, the d-d band of  $\text{Cu}^{2+}$  (vi) was completely absent. Hence, the complete reduction of  $\text{Cu}^{2+}$  ions was achieved in the CuMor10-450 sample and only the different reduced copper species were observed.

Unlike most other samples, CuMor10 demonstrates a well-resolved maximum (ii) at 250 nm that develops from the shoulder of CuMor10-150 to the well-pronounced peak of CuMor10-250-CuMor10-450 (Fig. 12). Feature (iii) contributes approximately in equal measure to all the spectra, while feature (iv) is better resolved for the CuMor10-450 sample. The plasmon resonance band (v) shows a complicated development, increasing in intensity from CuMor10-150 to CuMor10-250, followed by a fall in intensity and then another increase from CuMor10-350 to CuMor10-450, in line with a remarkable change in the shape of this maximum, degenerating from a peak into a broad step-like feature. This change of shape can provide evidence that the copper particles formed at low reduction temperatures in the interior of mordenite crystals, are formed on their exterior parts at higher temperatures. This variation of particle positions can be explained by the increased mobility of copper atoms at high temperatures, which favors their aggregation into the particles on the outer surface of microcrystals. These areas

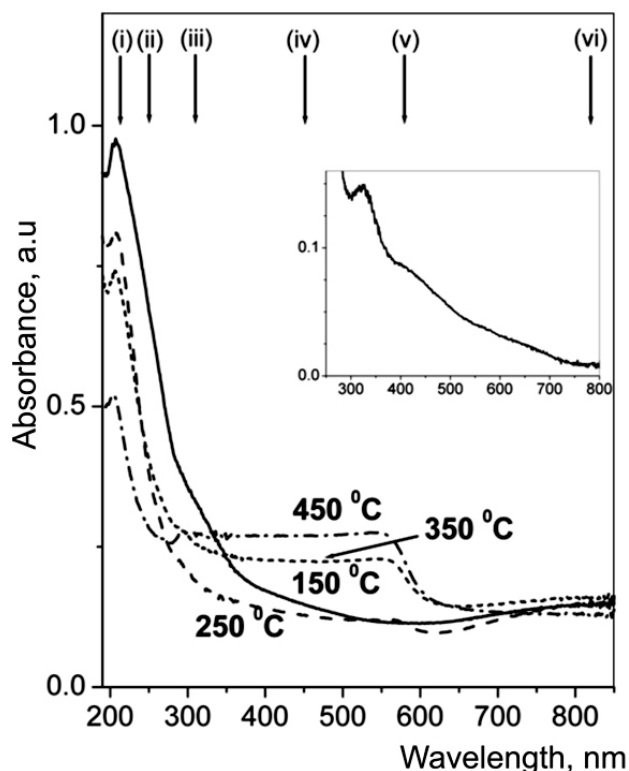


FIGURE 15. Absorption spectra of CuMor30 reduced at different temperatures.

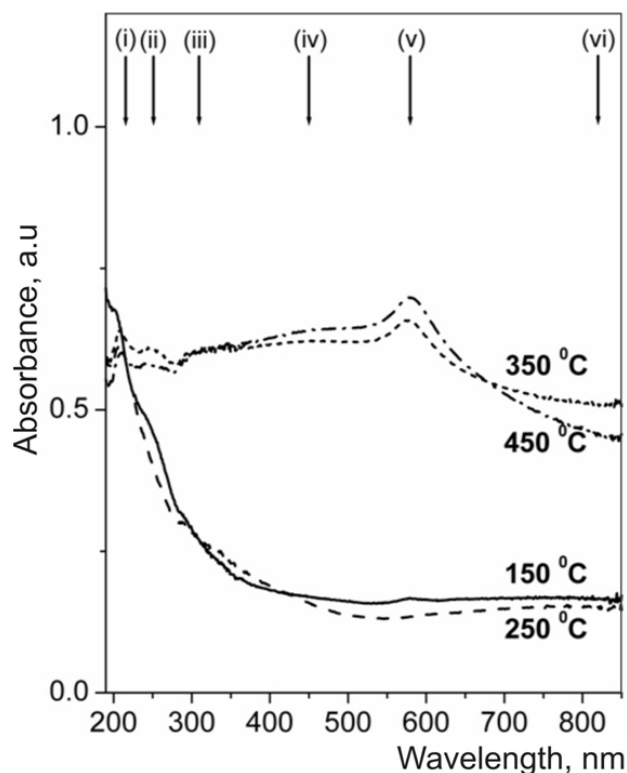


FIGURE 16. Absorption spectra of CuMor206 reduced at different temperatures.

provide an environment with lower dielectric constants than those of mesopores in the interior of zeolite [22].

It should here be mentioned that this complicated evolution of the Cu(0) plasmon band (v) at different reduction temperatures occurs only in CuMor10. Other mordenites result just in one type of feature, either a maximum (CuMor206, Fig. 16) or a shoulder (CuMor30, Fig. 15), and in some cases (CuMor15, Fig. 14) the feature does not appear at all. Thus, this peculiarity of the CuMor10 sample may be associated with a specific distribution of acid sites: only this sample demonstrates clearly the bimodal peak of ammonia TPD (Fig. 3). It seems that the sites with lower acidity favor the reduction of copper into Cu(0) located inside the mordenite matrix, while higher acidity give rise to migration of reduced copper onto the outer surface. The highest acidity (CuMor15) prevents particle formation completely. In fact, the highest contribution of acid sites in the  $pK_a$  range 5.0-5.7 ( $1.08 \mu\text{mol}/\text{m}^2$ ) is observed for HMor10, while for HMor15 and HMor30 the greatest contributions are due to BAS with  $pK_a$  1.5-2.3 ( $2.68 \mu\text{mol}/\text{m}^2$ ) and  $pK_a$  1.8-3.4 ( $1.84 \mu\text{mol}/\text{m}^2$ ), respectively (Table III). The two ammonia TPD peaks at 490 K and 660 K (Fig. 3) were recorded for HMor10, which corresponds to the two distinct acid sites. The weak acid sites in HMor10 provides for more efficient copper incorporation and reduction starting at 150°C, while the strong acid sites assist the appearance of intermediate reduced Cu<sup>+</sup> species.

### 3.4.2. DRS of the reduced CuMor15

The spectra of the CuMor15 samples (Fig. 14) did not show efficient reduction of copper. Indeed, noticeable bands (i) and (vi) belonging to Cu<sup>2+</sup> ions were observed for all CuMor15 samples except for CuMor15-150. The band (ii) at 250 nm due to Cu<sup>+</sup> species discussed above (Sec. 3.3) was not detected clearly; nevertheless, it may have been hidden as a weak shoulder interfering with the strong peak at 210 nm, especially for CuMor15-250.

The sample reduced under mild conditions, CuMor15-150, revealed a very broad descent down to the end of the available scale (Fig. 14). Similar features in absorption of solids are sometimes observed when a number of absorption mechanisms exist, and an absorption coefficient usually grows with photon energy. These absorption mechanisms in our case may be attributed to the presence of different intermediates of reduced copper. However, increasing temperature suppressed the formation of these species. Their features are not apparent in the spectra of other CuMor (Figs. 13, 15, 16). Nevertheless, this type of absorption may be extracted for CuMor10-150 and to a lesser extent for CuMor30-150 samples. Since initial HMor15 zeolite has the maximum number of acid sites with the higher acidity, high acidity probably prevents the efficient reduction of Cu(II) to produce copper nanoparticles.

It is of interest to include in the interpretation of this broad absorption the possibility of formation of small copper clusters. The mild reduction conditions can favor formation of these less stable species as compared with that of larger nanoparticles. For example, 8-atomic clusters Ag<sub>8</sub> are easily stabilized in the case of Ag-exchanged mordenites, and the mild reduction conditions correspond to the appearance of Ag<sub>8</sub> clusters rather than of the larger silver nanoparticles [15]; however, in the case of copper in zeolites no unambiguous indication has been made to this date [45]. Successful stabilization of the clusters of definite nuclearity is conditioned by their fitting into the mordenite channels with cross-section of 0.65×0.70 nm [4,21]. In the case of copper this good fitting requirement of Cu<sub>8</sub> isomers is violated since the possible size of corresponding copper clusters should be less than the size of silver clusters of the same nuclearity due to the smaller size of copper atom. Probably, copper clusters of the higher nuclearity could fit into the mordenite channel. In the CuMor15-150 spectrum there is a weak feature in the range 300-350 nm, attribution of which should be other than species (iii) enumerated above for CuMor samples. This weak maximum (CuMor15-150, Fig. 14) may be considered as the absorption of one of the possible Cu<sub>n</sub> copper clusters; however, the data on direct assignment are still disputable. We can only note that the bands at 280, 375, 450 nm [46] and 355, 375, 410 nm [47] were assigned to different low-stable copper species like Cu<sub>n</sub><sup>x+</sup>, formed in Cu<sup>2+</sup>-containing solutions, and a number of maxima in the range 300 – 550 nm were associated with Cu<sub>n</sub> clusters stabilized in matrices of rare gases [48,49].

### 3.4.3. DRS of the reduced CuMor30

The further increase of MR leads to a modification of the optical appearance of the copper reduced forms (Fig. 15). First of all, the plasma resonance peak (v) corresponding to the copper nanoparticles is developed; however, in this case it has a step-like shape rather than a well-developed maximum. This shoulder has been assigned to very small copper particles (with radii less than 10 nm) [22,50]. In the case of CuMor30 this feature appears at the reduction temperature of 250°C and regularly rises with increasing temperature. In the case of CuMor30-450, the spectrum in the range 300-550 nm has an absorption plateau with remarkably complex structure that is difficult to interpret (see Fig. 15) starting from the plasmon resonance shoulder. For the samples CuMor10 (Fig. 13) and CuMor206 (Fig. 16) weak maxima (iii) and (iv) related to the copper interband transitions are observed in this range in line with the plasmon resonance [51]. Meanwhile, for this sample all spectra except for CuMor30-450 include noticeable bands (i) and (vi) of Cu<sup>2+</sup> ions. The feature (ii) at ~250 nm related to the Cu<sup>+</sup> state is hidden as a shoulder on the slope of the intense 210 nm peak (i). Thus, this composition of the mordenite does not favor easy and complete reduction of Cu(II) to Cu(0).

The region (iii) 300-350 nm shows some weak features in the curves corresponding to all reduction temperatures (Fig. 15). For the samples reduced under high temperatures they look very similar to satellites to the plasmon resonance band due to interband transitions in copper. However, the CuMor30-150 sample that reveals no plasmon resonance shows a feature of particular interest in this region. The inset in Fig. 15 with the subtracted spectrum undoubtedly evidences that, for this sample, the maximum occurs at 322 nm. A similar peak is observed in the CuMor15-150 sample (Fig. 14) but with higher intensity. This peak may be associated with small copper clusters formed under mild reduction conditions, as well as with the CuMor15-150 sample. These samples, HMor15 and HMor30, are similar in the strength of active acid sites and copper ion exchange capacity. The lower concentration of the acid sites and their lower pK<sub>a</sub> for HMor30 than for HMor15 explains the less expressed spectral feature at 322 nm. This observation also supports the view that cluster formation may be connected with the acid sites of high strength.

### 3.4.4. DRS of the reduced CuMor206

Spectra of this sample can be divided into two distinct types: (A) 150 and 250°C and (B) 350 and 450°C (Fig. 16). These types are clearly distinguished throughout the whole spectral range. In the spectra of the A-type absorption band of Cu<sup>2+</sup>*d* – *d* transitions the feature (vi) is developed at the trace level. The minor feature (v) from the copper nanoparticles only appears weakly in the CuMor206-150 spectra. The weak shoulder (ii) at ~250 nm is developed in the CuMor206-150 spectrum but is absent from the CuMor206-

250 sample. The feature (i) at 210 nm can be distinguished as a shoulder in the spectra, and absorption continues to increase to the limit of the spectral range. It is possible to infer from the absence of the typical features both for Cu(II) and for any reduced species that practically all Cu(II) is reduced in the A-type samples, but these reduced forms have absorbance that does not appear in the accessible spectral range, probably at  $\lambda < 190$  nm.

Spectra of the B-type show the well-resolved plasmon resonance band (v) accompanied by two bands (iii) and (iv). The weak peak (ii) of Cu<sup>+</sup> at 250 nm is well resolved. Hence, a significant part of Cu(II) in B-type of samples is reduced to metal nanoparticles. An important difference between B- and A-type spectra is the intense background absorbance throughout the entire spectral interval under study. This background may be associated with the structureless absorbance by large metal particles and aggregates of larger size [52].

## 3.5. General analysis of the samples with different MR

The preparation procedure and composition of mordenite defines the nature and concentration of acid sites, secondary porosity and total surface area of zeolite matrices. Closer examination proved that with respect to variations in MR of mordenites, non-monotonic dependence is observed for: a) secondary porosity; b) total surface area; c) total acidity; d) relative amount of different types of acid sites, *i.e.* their pK<sub>a</sub> and surface concentrations.

Depending on these variations of mordenite properties changes are observed for: 1) the amount of incorporated copper ions via ion-exchange; 2) the amount of Cu(II) ions in the set of hydrated samples measured by EPR; 3) initial temperature of Cu(II) reduction with formation of nanoparticles; 4) the shape of plasmon resonance band of copper nanoparticles; and 5) the appearance of other reduced copper species.

The reduction temperature strongly influences the species of copper formed. All the above-mentioned factors provide changes in the final products. The nature of active acid sites can affect the positions of copper ions, their reactivity, and the behavior of final reduction products.

The TPD measurements (Fig. 3) allow us to separate acid sites into three different types, participating, presumably, in the process of copper incorporation and reduction. Surface concentration and pK<sub>a</sub> of the Brønsted acid sites revealed by titration measurements (Table III) correlate with TPD of ammonia and demonstrate complex dependence on MR regarding their appearance and acidity. In general, the following correlations may be found between the properties of acid sites occurring at different MR in the mordenites and the spectral appearance of the copper species formed as a result of hydrogen reduction:

In the samples CuMor15 and CuMor30 a large amount of strong acid sites (730 K peak in the TPD data) is present. A small fraction of these is occupied by copper ions after ion exchange (Table 2). This environment promotes reduction of Cu<sup>2+</sup> ions either to small copper clusters under

low-temperature (CuMor15-150, CuMor30-150), or to copper nanoparticles within the size range  $\sim 1$ -2 nm under high-temperature reduction (CuMor30-350, CuMor30-450). The high acid strength of these sites prevents the reduction of copper to metal, and the sample CuMor15 appears to be almost unreduced even at 450°C. Lower concentration of strong acid sites in HMor206 leads only to prevention of  $\text{Cu}^{2+}$  reduction at temperatures lower than 350°C.

Intermediate strength acid sites (660 K peak in the TPD data) bind copper ions in the CuMor10 and CuMor206 samples with less strength. The low temperatures are sufficient only for copper reduction to Cu(I), rather than to Cu(0), while with higher temperatures reduced copper species aggregate rapidly to form nanoparticles of  $\sim 5$ -10 nm. Plasmon resonance of the particles of this size range appears as a well developed band. The fine details of its contour are determined by particle location, environment, shape factor, etc. [53].

The weakest acid sites (490 K peak in the TPD data), presumably of a different nature, occur in considerable amounts in the CuMor10 sample only. Their nature is possibly connected with extra-framework aluminum atoms; this may explain their peculiar behavior. These sites bind copper ions weakly and copper nanoparticles with a well-pronounced plasmon resonance maximum are formed along the whole temperature range.

These three types of acid sites exist in protonated mordenite and, according to the findings above, contribute in very different manner to copper reducibility. The spectroscopic data on the state of  $\text{Cu}^{2+}$  ions in the Cu-exchanged forms of mordenites collected within the framework of this work allow us to separate different copper adsorption sites only partially. One sub-band at  $\sim 620$  nm may be extracted from the broad optical absorption band related to  $d-d$  transition in  $\text{Cu}^{2+}$ . It occurs in the case of CuMor10 possessing the featured acid sites and this sub-band may be associated with these weakest acid sites, which do not occur in Cu-exchanged mordenites with other MR. The other two acid sites of higher strength are associated with the framework T-positions of aluminum and probably produce two main positions for copper ion absorption. Two copper sites were determined by Cheetham et al. using direct X-ray analysis of a single crystal of mordenite with MR=28.8 (close to our MR=30) [19]. One site coordinated with oxygen in the elliptical 8-rings, the other (octahedral) within the main 12-ring channel.

Since the crystal structure of mordenites with  $15 \leq \text{MR} \leq 206$  is practically the same (Sec. 3.1), we propose that similar positions can be realized for other mordenites, not only for MR $\sim$ 30 (except for MR=10 which has, as was stated above, the possible additional position for ion-exchanged ions). However, under our experimental conditions mordenites are capable of exchanging only low percentages of Cu (Table II). These low values mean that only one of the two copper positions can be active, and only one type of acid center develops the main activity in HMor30. The second type makes a much lower but still evident contribution, as seen from the change in the low-temperature

side of the TPD curve discussed in Sec. 3.1. Thus, it may be proposed that the positions within the 8-member ring are responsible for Cu absorption in CuMor15 and CuMor30.

HMor206, in contrast, makes its main contribution to the TPD at intermediate temperatures. Thus, an increase of the MR value from 30 to 206 changes the type of copper site that is most active. In Mor206 with its lower Al content, this site is more stable and provides higher ion-exchange ability. The site is probably located in the 12-member ring. The less the strength of the active centers the more complete the ion-exchange. 12-ring positions are weaker than 8-ring positions. This is to say, a strong acid keeps cations worse. This fact is common in the chemistry of aqueous solutions. Due to the higher degree of ion-exchange, both types of centers are probably occupied, at least partially. The variability in  $\text{Cu}^{2+}$  bonding is manifested in the reduction process: strong acidity and the weaker bond of copper ions with the zeolite framework (8-rings) prevent effective reduction, but lower acidity promotes the reduction (for copper ions sitting within 12-rings).

The significant effect of hydrogen reduction temperature on copper reducibility may also be explained from this viewpoint. Dehydration of mordenites used in this work may be extended to up to 200-300°C depending on the MR [10,22] and makes additional changes in the copper absorption centers. Instead of two copper positions within the 8- and 12-rings, in dehydrated mordenite (up to 510°C) three positions were detected [19]: the position within the 8-ring equal, but the 12-ring can now contain two positions. On the basis of these crystallographic data for original and dehydrated mordenites with copper, it may be speculated that the reduction temperature has little effect when 8-ring positions are active, but the higher effect of temperature would be for copper located within the 12-ring. Variable reactivity of copper in other zeolites depending on its crystallographic positions has also been noted in other studies [20,54-56]. Probably, HMor206 incorporates copper into 12-rings, HMor30 and HMor15 incorporate it into the 8-ring, and HMor10, in addition to the positions in the 12-ring, has the extra-framework copper (see above, Sec. 3.1 and Ref. 57). The maximum reducibility from experimental data considered in Secs. 3.4 can be attained when copper ions are in the more open 12-ring, and the minimum would be for copper in the 8-ring.

#### 4. Conclusions

Copper incorporated by ion exchange into mordenites with various  $\text{SiO}_2/\text{Al}_2\text{O}_3$  values (MR), and therefore variable acid properties, can be reduced by heat treatment in hydrogen with the concomitant production of a number of species: Cu(I) states, copper nanoparticles of different size and localization in the mordenite, and small copper clusters. The spectral appearance of these species in the samples recorded by EPR and DRS of the Cu-containing hydrated, as well as reduced mordenites strongly depends on the value of MR and on the

reduction temperature. MR serves as the key factor that regulates both concentration and strength of the acid sites. The following correlations were obtained:

- (i) the mordenite sample with the lowest acid strength, MR=10, in part due to the presence of extra-framework aluminum, provided efficient copper reduction; and the size of the nanoparticles produced grows with the reduction temperature;
- (ii) the most acid sites (both in concentration and strength) for MR=15 and 30 prevented copper reduction, but, only in these cases, under mild conditions, the possibility of small copper cluster formation was noted in the optical spectra;
- (iii) in the case of acid sites of medium strength in the highly dealuminated mordenite with MR=206, copper reduction proceeded effectively only at high temperatures, and nanoparticles with the pronounced plasmon resonance band were formed.

The clear difference in behavior of MR-variable mordenites with respect to copper reducibility was interpreted as being due to exchange of Cu<sup>2+</sup> ions into different sites, depending upon the amount of aluminum present in the mordenite (controlled by MR ratio). The more active (and, correspondingly, the more reducible) copper enters the positions in the 8-rings, and the less active copper appears in the 12-rings.

Secondary porosity plays a significant role among the factors regulating locations where copper nanoparticle formation occurs, in media with varying dielectric functions.

The material of this work contributes to the understanding of copper behavior in zeolites and catalysts by allowing us to propose MR as an efficient tool in metal state regulation, which is an important factor in catalytic activity and selectivity. Various optical features of zeolites with copper nanoparticles may be proposed for the design of new optical materials with absorption tuned by the ionic properties of the matrix.

## Acknowledgments

We greatly benefited from many discussions and collaborations with Dr. Yoshihiro Sugi, Dr. Karl Seff, Dr. Robert Marzke and Dr. Sergey Romanov. We wish to thank Jose Victor Tamariz Flores for his experimental work on measurements of Cu content. The authors would also like to express their gratitude to Francisco Ruiz, Eloisa Aparicio, Eric Flores and Juan Peralta for the invaluable technical support. The research reported in this paper was supported by grant IN114603 3 from UNAM-PAPIIT, grant 102907, CONACYT, Mexico, and grant RFBR 090300347-a, Russia. The authors F. Chavez Rivas and R. Zamorano Ulloa acknowledge support from COFAA-IPN-Mexico.

1. B. C. Gates, *Chem. Rev.* **95** (1995) 511.
2. K. Seff, and T. Sun, *Chem. Rev.* **94** (1994) 857.
3. G. Stucky, and J. Mac Dougall, *Science* **247** (1990) 669.
4. V.S. Gurin, N.E. Bogdanchikova, and V.P. Petranovskii, *J. Phys. Chem. B* **104** (2000) 12105.
5. P.P. Edwards, P.A. Anderson, and J.M. Thomas, *Acc. Chem. Res.* **29** (1996) 23.
6. Yu.A. Alekseev, V. Bogomolov, T. Zhukova, V. Petranovskii, and S. Kholodkevich, *Sov. Phys. Solid State* **24** (1982) 1384.
7. T. Sun, K. Seff, N.H. Heo, and V. Petranovskii, *Science* **259** (1993) 495.
8. Y. Park, Y.S. Lee, and K.B. Yoon, *J. Am. Chem. Soc.* **115** (1993) 12220.
9. J. Ogden, N. Bogdanchikova, J. Corker, and V. Petranovskii, *Eur. J. Phys. D* **9** (1999) 605.
10. D. W. Breck, *Zeolite Molecular Sieves. Structure, Chemistry and Use* (A Wiley-Interscience Publication, John Wiley & Sons, New York, 1974).
11. Atlas of Zeolite Structure Types, 5<sup>th</sup> revised edition, (Ch. Baerlocher, W. M. Meier and D. H. Olson, Eds. 2000). Available on-line: <http://www.iza-structure.org/databases/>
12. H. Yahiro, and M. Iwamoto, *Appl. Catal. A* **222** (2001) 163.
13. C. Torre-Abreu, C. Henriques, F.R. Ribeiro, G. Delahay, and M.F. Ribeiro, *Catal. Today* **54** (1999) 407.
14. V.I. Parvulescu, P. Grange, and B. Delmon, *Catal. Today* **46** (1998) 233.
15. N. Bogdanchikova, V. Petranovskii, R. Machorro, Y. Sugi, V.M. Soto, and S. Fuentes, *Appl. Surf. Sci.* **150** (1999) 58.
16. N. Bogdanchikova, V. Petranovskii, S. Fuentes, E. Paukshtis, Y. Sugi, and A. Licea-Claverie, *Mater. Sci. Eng. A* **276** (2000) 236.
17. S.Y. Chung, S.H. Oh, M.H. Kim, I.S. Nam, and Y.G. Kim, *Catal. Today* **54** (1999) 521.
18. B.R. Goodman, K.C. Hass, W.F. Schneider, and J.B. Adams, *Catal. Lett.* **68** (2000) 85.
19. M.P. Attfield, S.J. Weigel, and A.K. Cheetham, *J. Catal.* **170** (1997) 227.
20. P.A. Jacobs, W. de Wilde, R.A. Shoonheidt, and J.B. Uytterhoven, *J. Chem. Soc. Faraday Trans. I* **72** (1976) 1221.
21. V. Gurin, N. Bogdanchikova, and V. Petranovskii, *Mater. Sci. Eng. C* **18** (2001) 37.
22. V. Petranovskii, V. Gurin, N. Bogdanchikova, A. Licea-Claverie, Y. Sugi, and E. Stoyanov, *Mater. Sci. Eng. A* **332** (2002) 174.
23. N. Katada, H. Igi, J.-H. Kim, and M. Niwa, *J. Phys. Chem. B* **101** (1997) 5969.

24. H. Igi, N. Katada, M. Niwa, in: M.M.J. Treacy, B.K. Marcus, M.E. Bisher, J.B. Higgins, *Materials Research Society* **4** (1999) 2643.
25. K. S. W. Sing *et al.*, *Pure Appl. Chem.* **603** (1985) 57.
26. V. Petranovskii *et al.*, *Stud. Surf. Sci. Catal.* **142** (2002) 815.
27. J. W. Akitt, *Progress in NMR Spectr.* **21** (1989) 1.
28. N. Katada, Y. Kageyama, and M. Niwa, *J. Phys. Chem. B* **104** (2000) 7561.
29. S. C. Larsen, A., Aylor, A. T., Bell, and J. A. Reimer, *J. Phys. Chem.* **98** (1994) 11533.
30. P. J. Carl, and S. C. Larsen, *J. Catal.* **182** (1999) 208.
31. P. J. Carl, and S. C. Larsen, *J. Phys. Chem. B.* **104** (2000) 6568.
32. W. Froncisz, and S. H. James, *J. Chem. Phys.* **73** (1980) 3123.
33. C. Oliva, *et al.*, *J. Chem. Soc., Faraday Trans.* **93** (1997) 2603.
34. F. Chavez Rivas, V. Petranovskii and R. Zamorano Ulloa, *Rev. Mex. Fis.* **56** (2010) 328.
35. E. Castañeda Miranda, Tesis Licenciatura "Caracterización de la zeolita Cu-ZSM5 por EPR y DRX para razones molares de 20 y 30". Febrero del 2005. ESFM-IPN.
36. A.B.P. Lever, *Inorganic Electronic Spectroscopy*, 2nd Edition, Elsevier, Amsterdam, 1984.
37. F.S. Hadzhieva, V.F. Anufrienko, T.M. Yurieva, V.N. Vorobiev, T.P. Minyukova, *React. Kinet. Catal. Lett.* **30** (1986) 85.
38. G.T. Palomino, P. Fisticaro, S. Borgida, A. Zecchina, E. Giannello, and C. Lamberti, *J. Phys. Chem. B* **104** (2000) 4064.
39. R.M. Friedman, J.J. Freeman, and F.W. Lytle, *J. Catal.* **55** (1978) 10.
40. B.J. Hathaway, *Coord. Chem. Rev.* **52** (1983) 87.
41. C.J. Ballhausen, *Introduction to ligand field theory*. (McGraw-Hill Book Company Inc., New York, 1963).
42. R. Debnath and K.S. Das, *Chem. Phys. Lett.* **155** (1989) 52.
43. P.D. Yang *et al.*, *Science* **282** (1998) 2244.
44. H.T. Wang, Z.B. Wang, L.M. Huang, A. Mitra, B. Holmberg, and Y.S. Yan, *J. Mater. Chem.* **11** (2001) 2307.
45. Y. Kuroda, S. Konno, Y. Yoshikawa, H. Maeda, Y. Kubozono, H. Hamano, R. Kumashiro, and M. Nagao, *J. Chem. Soc.-Faraday Trans.* **93** (1997) 2125.
46. B.G. Ershov, E. Janata, and A. Henglein, *Radiat. Phys. Chem.* **39** (1992) 123.
47. J. Khatouri, M. Mostafavi, J. Amblard, and J. Belloni, *Chem. Phys. Lett.* **191** (1992) 351.
48. G.A. Ozin, H. Huber, D. McIntosh, S. Mitchell, J.G. Norman Jr., and L. Noodleman, *J. Am. Chem. Soc.* **101** (1979) 3504.
49. G.A. Ozin, S. Mitchell, D.F. McIntosh, S.M. Mattar, and J. Garcia-Prieto, *J. Phys. Chem.* **87** (1983) 4651.
50. I. Lisiecki, and M.P. Pileni, *J. Phys. Chem.* **99** (1995) 5077.
51. J.F. Janak, A.R. Williams, V.L. Moruzzi, *Phys. Rev. B* **11** (1975) 1522.
52. Y.I. Petrov. Clusters and Small Particles, *Nauka, Moscow* (1986).
53. U. Kreibig, M. Vollmer, *Optical Properties of Metal Clusters* (Springer-Verlag, Berlin, 1995).
54. M.P. Attfield, S.J. Weigel, and A.K. Cheetham *J. Catal.* **172** (1997) 274.
55. B. Wichterlova, J. Dedecek, Z. Sobalyk, A. Vondrova, and K. Kliery, *J. Catal.* **169** (1997) 194.
56. Y. Kuroda, Y. Yoshikawa, S. Emura, R. Kumashiro, and M. Nagao, *J. Phys. Chem. B* **103** (1999) 2155.
57. M. Niwa, K. Suzuki, N. Katada, T. Kanougi, and T. Atoguchi, *J. Phys. Chem. B* **109** (2005) 18749.